CrossMark

J. Fluid Mech. (2015), *vol.* 775, *pp.* 24–52. © Cambridge University Press 2015
doi:10.1017/jfm.2015.289

Computational study of granular shear flows of dry flexible fibres using the discrete element method

Y. Guo[1],†, C. Wassgren[2], B. Hancock[3], W. Ketterhagen[3] and J. Curtis[1]

[1]Chemical Engineering Department, University of Florida, Gainesville, FL 32611, USA

[2]School of Mechanical Engineering, Purdue University, West Lafayette, IN 47907, USA

[3]Pfizer, Inc., Groton, CT 06340, USA

(Received 1 November 2014; revised 16 April 2015; accepted 18 May 2015;
first published online 16 June 2015)

In this study, shear flows of dry flexible fibres are numerically modelled using the discrete element method (DEM), and the effects of fibre properties on the flow behaviour and solid-phase stresses are explored. In the DEM simulations, a fibre is formed by connecting a number of spheres in a straight line using deformable and elastic bonds. The forces and moments induced by the bond deformation resist the relative normal, tangential, bending and torsional movements between two bonded spheres. The bond or deforming stiffness determines the flexibility of the fibres and the bond damping accounts for the energy dissipation in the fibre vibration. The simulation results show that elastically bonded fibres have smaller effective coefficients of restitution than rigidly connected fibres. Thus, smaller solid-phase stresses are obtained for flexible fibres, particularly with bond damping, compared with rigid fibres. Frictionless fibres tend to align with a small angle from the flow direction as the solid volume fraction increases, and fibre deformation is minimized due to the alignment. However, jamming, with a corresponding sharp stress increase, large fibre deformation and dense contact force network, occurs for fibres with friction at high solid volume fractions. It is also found that jamming is more prevalent in dense flows with larger fibre friction coefficient, rougher surface, larger stiffness and larger aspect ratio.

Key words: complex fluids, granular media

1. Introduction

A large number of studies have focused on understanding granular flows of rigid spherical and non-spherical particles. However, the flow of dry flexible fibres has not yet been comprehensively investigated despite its significance, and hence it is the focus of the present work. As an introduction, continuum-based theories of granular flows are reviewed in this section since these theories provide the foundation for the studies and understanding of discrete granular system dynamics. As flexible fibres are normally thin and long, the effect of particle elongation on packing and flow is also discussed. In the last part of this section, the current research status on flexible fibres is presented and the content of the present work is outlined.

† Email address for correspondence: guoyu03@gmail.com

https://doi.org/10.1017/jfm.2015.289 Published online by Cambridge University Press

1.1. *Continuum-based description of granular flows*

Granular material, recognized as an assembly of discrete solid particles, can behave like a gas, a liquid, a solid or a mixture of these phases under different conditions. As a result, continuum-based theories, such as fluid mechanics and solid mechanics, have been used to describe the complex mechanical behaviour of granular materials. Granular kinetic theory is a popular one among such methods and was introduced to predict dilute and moderately dense granular flows in which the motion of individual particles is analogous to the thermal motion of molecules in gases, i.e. the particle–particle collisions are binary and instantaneous (Lun *et al.* 1984; Goldshtein & Shapiro 1995; Montanero *et al.* 1999; Goldhirsch 2003). According to granular kinetic theory, the bulk solid-phase stress tensor is a function of $\rho d_p^2 \gamma^2$, the coefficient of restitution e and the solid volume fraction v. The term $\rho d_p^2 \gamma^2$, in which ρ and d_p are the particle density and diameter respectively and γ is the shear strain rate, represents the particle kinetic energy. The coefficient of restitution e, defined as the ratio of postcollisional to precollisional relative velocities between two contacting particles, characterizes the dissipation of kinetic energy due to damping in a collision when e is less than one. The solid volume fraction v has a strong influence on the collision frequency, particle velocity fluctuations and interparticle contact forces.

In dense granular flows, the multiple long-lasting collisions become dominant (Campbell 2002, 2005; Jenkins 2006). As a result, the gas-based kinetic theory, established on the assumption of binary instantaneous collisions, cannot be directly used to capture the features of dense flows. Johnson & Jackson (1987), Johnson, Nott & Jackson (1990) suggested the addition of a frictional contribution to the granular kinetic theory stress to incorporate the effect of interparticle tangential contact forces. In order to determine the frictional term in the constitutive equations, Jop, Forterre & Pouliquen (2006) performed theoretical and experimental studies of granular flows on a pile between rough sidewalls, showing that the bulk density and bulk friction coefficient (i.e. the ratio of shear to normal stresses of a bulk material) are functions of the inertial number,

$$I = \gamma d_p \sqrt{\rho}/P, \tag{1.1}$$

in which P is the pressure. The inertial number I was interpreted as the ratio of the pressure-induced inertial time scale, $d_p\sqrt{\rho}/P$, and the time scale of deformation, γ^{-1}. Using the inertial number as a key parameter, Pouliquen & Forterre (2009) proposed a non-local model to describe the flow of granular media as a self-activated process, in which particle rearrangement at one position is triggered by the stress fluctuations induced by rearrangements elsewhere in the bulk material. This work was an attempt to unify the quasi-static regime (shear-rate-independent) and inertial regime (shear-rate-dependent), and predictions from the developed model are consistent with the experimental observations of granular flows down inclined planes and plane shear under gravity.

Other dense phase continuum theories have also been developed. Based on the coarse-graining (spatial-smoothing) formulation as first proposed by Babic (1997), Goldhirsch (2010) developed a set of explicit and closed expressions for the stress and couple-stress fields for discrete systems in terms of the constituents' degrees of freedom and interactions. Weinhart *et al.* (2012) extended Goldhirsch's theory by developing an expression for the stress tensor near external boundaries to account for the boundary interaction forces, and they obtained an excellent prediction of the stress profile close to the boundary using the developed theory. Recently, Weinhart *et al.* (2013) examined the influences of the local stress anisotropy and structural anisotropy

https://doi.org/10.1017/jfm.2015.289 Published online by Cambridge University Press

on the flow rheology by performing discrete element method (DEM) simulations of frictional granular flows down an inclined rough chute. They developed an anisotropic local constitutive model for a prediction of the granular flow behaviour in general flow situations. Besides the frictional interaction, Campbell (2002, 2005, 2006) also recognized the importance of particle elastic properties in dense flows and proposed a constitutive framework based on the dimensionless stresses $\sigma d_p/k$ and dimensionless stiffness $k/(\rho d_p^3\gamma^2)$, in which k represents the interparticle contact stiffness. From the DEM simulations of granular shear flows, Campbell found that at large solid volume fractions, the stress increases linearly with the contact stiffness k at small shear rates (elastic quasi-static regime) and increases linearly with the square root of the contact stiffness $\sqrt{k}$ at large shear rates (elastic inertial regime).

1.2. *Effect of particle elongation*

Particle shape, which determines the microstructure of a bulk material, has a remarkable impact on granular packing and flow. As the particles become more elongated, the bulk density generally decreases and the coordination number increases (Guises *et al.* 2009; Wouterse, Luding & Philipse 2009). In addition, particle elongation may cause regions of particle alignment (Lumay & Vandewalle 2006), leading to force transmission in the lateral direction being less favoured than transfer in the normal direction. As a result, force saturation is hindered (Hidalgo *et al.* 2010; Acevedo *et al.* 2014). In a significant attempt to describe non-spherical particle flows, Huthmann, Aspelmeier & Zippelius (1999) developed a kinetic theory of hard needle-shaped particles, which is strictly restricted to low and moderate solid fractions due to the assumptions of binary collisions and a homogeneous cooling state. In a dense granular flow, rotation of elongated particles increases the collision frequency. Thus, it is observed that the shear strength, dilatancy and coordination number all increase as particles become more elongated in two-dimensional biaxial compression tests (Azéma & Radjaï 2010) and in stress-controlled shear flows (Peña, García-Rojo & Herrmann 2007).

Wegner *et al.* (2014), in their shear cell experiments on spherical and elongated grains, observed the existence of a competition of dilatancy effects with orientational and positional ordering which both tend to increase the packing density. Increase in particle elongation causes more pronounced shear-induced ordering, leading to weaker dilatancy. In Couette flows of circular disks (Cleary 2008), the solid volume fraction was observed to be large at the centre of the channel and small at the walls, with the granular temperature small at the centre and large at the walls. However, the distributions of solid volume fraction and granular temperature become more uniform as particles become more elongated (using superquadric particle shapes). In addition, larger normal and shear stresses are obtained for more elongated particles. Recently, Guo *et al.* (2012, 2013*a*) developed a DEM code for true cylindrical particles and applied it to simulate shear flows of rigid elongated particles in the absence of fluid media. They systematically studied the effects of particle elongation, surface roughness and friction, coefficient of restitution and contact stiffness on the granular flow pattern, particle orientational alignment and particle-phase stress.

1.3. *Flows of flexible fibrous particles*

Biomass materials (e.g. corn stover, wheat straw and wood chips) are believed to be a future source of fuel. For economical production of biomass fuels, fibrous biomass particles need to be processed in large volume and at a high concentration. These

https://doi.org/10.1017/jfm.2015.289 Published online by Cambridge University Press

highly concentrated biomass materials normally possess high effective viscosity and have non-Newtonian flow behaviour. As a result, effective handling and processing of biomass materials is a significant technical challenge in energy-related industries. For a better understanding of biomass material flow behaviour, Stickel *et al.* (2009) adopted a variety of instruments (vanes, roughened plates and a torque rheometer) to measure the rheological properties of corn stover that had been pretreated using dilute acid. Corn stover slurries at concentrations of up to 30 % insoluble solids by mass were found to be strongly shear-thinning and had a larger yield stress at a higher concentration. Lavenson *et al.* (2011) measured velocity profiles and yield stresses of pretreated corn stover and delignified commercial cellulose suspensions at mass concentrations of 5–15 % in pipe flows using a combined method of magnetic resonance imaging and pressure drop measurement. They found that yield stress is determined by mass concentration, fibre length, fibre pretreatment, fibre type and fibre size distribution.

Experimental work can provide important macroscopic rheological information such as yield stress, viscosity and elastic/shear moduli of a bulk fibre system. However, fibre-scale information, such as fibre orientation, deformation, spatial distribution, interfibre contacts and network formation, which is difficult to obtain experimentally, is important for an understanding of the correlation of macroscopic behaviour and microscopic properties. Fortunately, computer modelling has proven to be an effective tool for providing such microscopic information (Yamamoto & Matsuoka 1993; Ross & Klingenberg 1997; Ning & Melrose 1999; Lindstrom & Uesaka 2007; Wu & Aidun 2010; Langston, Kennedy & Constantin 2015). A brief comparison of several existing numerical fibre models has been made by Guo *et al.* (2013*b*). Previous computational studies of flexible fibres mainly focused on liquid–fibre two-phase suspensions with a low solid concentration (<15 % by volume) and infrequent interfibre contacts. Knowledge and numerical modelling of highly concentrated fibre slurries and a single-phase fibre flow are largely lacking. In energy plants using biomass fuels, low moisture content or dry biomass materials are preferable to very wet materials in storage and combustion due to relatively better flowability and higher net energy density. Hence, extra water content in wet materials usually needs to be driven off for storage and combustion. As a result, handling of dry fibrous materials (using screw conveyors, belt conveyors, bucket elevators, pneumatic conveying systems, etc.) is encountered when moving product in and out of biomass storage and combustion systems. Despite the application significance, the flow of dry flexible fibres, especially at high solid volume fractions, has not yet been comprehensively investigated.

As an attempt to understand the effects of fibre flexibility, a damped flexible fibre model based on the DEM method (Guo *et al.* 2013*b*) is employed in the present work to simulate shear flows of dry flexible fibres in the absence of fluid media and gravity. Flows over a range of solid volume fractions from 0.025 to 0.47 (close to the packing limit of the model fibres) are examined. The effects of fibre properties, such as bond or deforming stiffness, bond damping, friction coefficient, surface roughness and aspect ratio, on the effective coefficient of restitution, fibre orientation, deformation, mechanical energy, solid-phase stress, apparent friction coefficient and coordination number have been studied.

2. Discrete element method modelling of shear flows of fibres

In this section, theoretical aspects and algorithms of the DEM-based flexible fibre model are first introduced. Next, the numerical model for shear flows of flexible fibres and the simulation parameters are described.

https://doi.org/10.1017/jfm.2015.289 Published online by Cambridge University Press

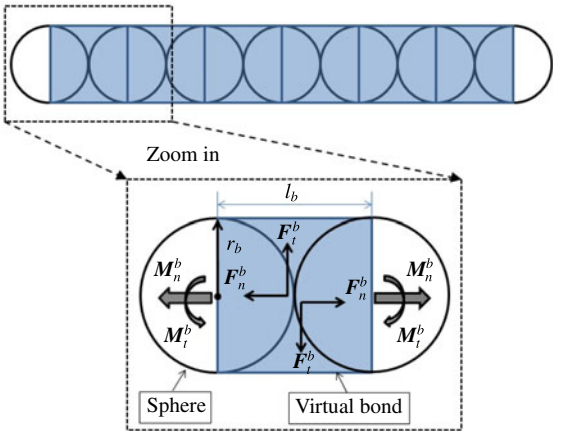


FIGURE 1. (Colour online) Illustration of the flexible fibre model (Guo *et al.* 2013*b*).

2.1. *Flexible fibre model*

The flexible fibre model used in this study has been described in our recent work (Guo *et al.* 2013*b*). In addition, a comprehensive validation of the mechanical responses of a single fibre, including bending, stretching/compressing and twisting deformation, has been made by comparing the model with analytical solutions (Guo *et al.* 2013*b*). For convenience, the model is also summarized here. A fibre is formed by connecting a number of identical spheres in a straight line using virtual elastic bonds, as shown in figure 1. Two ends of a single bond, which are fixed on the centres of two neighbouring spheres, translate and rotate with the spheres. Thus, the relative movement of constituent spheres leads to deformation of the bonds and also the fibre. In return, bond forces/moments are generated and exerted on the spheres to resist the deformation. According to the bonded-particle model by Potyondy & Cundall (2004), the bond forces and moments can be calculated incrementally as follows:

$$\mathrm{d}F_n^b = K_n^b\,\mathrm{d}\delta_n^b = \frac{E_b A}{l_b}\,\mathrm{d}\delta_n^b = \frac{E_b A}{l_b} v_n^r\,\mathrm{d}t, \tag{2.1}$$

$$\mathrm{d}F_t^b = K_t^b\,\mathrm{d}\delta_t^b = \frac{G_b A}{l_b}\,\mathrm{d}\delta_t^b = \frac{G_b A}{l_b} v_t^r\,\mathrm{d}t, \tag{2.2}$$

$$\mathrm{d}M_n^b = K_{tor}^b\,\mathrm{d}\theta_n^b = \frac{G_b I_p}{l_b}\,\mathrm{d}\theta_n^b = \frac{G_b I_p}{l_b}\omega_n^r\,\mathrm{d}t, \tag{2.3}$$

$$\mathrm{d}M_t^b = K_{ben}^b\,\mathrm{d}\theta_t^b = \frac{E_b I}{l_b}\,\mathrm{d}\theta_t^b = \frac{E_b I}{l_b}\omega_t^r\,\mathrm{d}t, \tag{2.4}$$

in which $\mathrm{d}F_n^b$, $\mathrm{d}F_t^b$, $\mathrm{d}M_n^b$ and $\mathrm{d}M_t^b$ are the incremental bond normal force, shear force, torsional moment and bending moment respectively, and $\mathrm{d}\delta_n^b$, $\mathrm{d}\delta_t^b$, $\mathrm{d}\theta_n^b$ and $d\theta_t^b$ are the incremental normal deformation, shear deformation, torsional (normal) angular deformation and bending (tangential) angular deformation respectively of the bond. Thus, K_n^b, K_t^b, K_{tor}^b and K_{ben}^b represent the normal, shear, torsional and bending stiffnesses respectively of the bond. The cylindrical bond of Young's modulus E_b and shear modulus G_b has a radius r_b, a length l_b, a cross sectional area $A = \pi r_b^2$, an area moment of inertia $I = \pi r_b^4/4$ and a polar area moment of inertia $I_p = \pi r_b^4/2$. In the present model, the bond radius r_b is assumed to be the same as the constituent sphere

https://doi.org/10.1017/jfm.2015.289 Published online by Cambridge University Press

radius r_s, and the bond Young's modulus E_b and shear modulus G_b are correlated through the Poisson's ratio $\zeta : E_b = 2(1+\zeta)G_b$. The virtual bond has no mass. The incremental bond deformation can be obtained from the product of the corresponding relative velocity between two bonded spheres (v_n^r, v_t^r, ω_n^r or ω_t^r) and the time step dt.

The movement of individual constituent spheres in each fibre-like particle is governed by Newton's second law of motion, i.e.

$$m_s \frac{\mathrm{d}^2 \boldsymbol{x}_s}{\mathrm{d}t^2} = \boldsymbol{F}^c + \boldsymbol{F}^b + m_s \boldsymbol{g} + \boldsymbol{F}_d^c + \boldsymbol{F}_d^b, \tag{2.5}$$

$$J_s \frac{\mathrm{d}^2 \boldsymbol{\theta}_s}{\mathrm{d}t^2} = \boldsymbol{M}^c + \boldsymbol{M}^b + \boldsymbol{M}_d^c + \boldsymbol{M}_d^b, \tag{2.6}$$

in which $\boldsymbol{x}_s$ and $\boldsymbol{\theta}_s$ are the translational displacement and angular displacement respectively of the sphere of mass m_s and moment of inertia $J_s = (2/5)m_s r_s^2$. The translational motion of the sphere is driven by the contact force $\boldsymbol{F}^c$ exerted by the spheres that are not bonded to it or come from a different composite particle, the bond force $\boldsymbol{F}^b$ exerted by the bonds connecting to it and the gravitational force $m_s\boldsymbol{g}$. The contact force between the spheres from two different composite particles $\boldsymbol{F}^c$ and the bond force $\boldsymbol{F}^b$ are calculated incrementally based on (2.1) and (2.2). The moment $\boldsymbol{M}^c$ arises from the tangential component of the contact force $\boldsymbol{F}^c$, and $\boldsymbol{M}^b$ represents the bond moment induced by the shearing, bending and twisting deformation of the bond. A contact force $\boldsymbol{F}^c$ can be decomposed into a normal force and a tangential force. The elastic normal force is computed based on the current normal overlap between two spheres using the Hertz model (Johnson 1985). The tangential interaction consists of static and sliding friction processes. For static friction, the tangential force depends on the current normal force and the tangential loading path according to the Mindlin–Deresiewicz theory (Thornton & Yin 1991). When the tangential force exceeds the product of the friction coefficient μ and the current normal contact force F_n^c, sliding friction occurs. The tangential force in the sliding process is equal to μF_n^c according to Coulombic sliding friction theory.

In (2.5), the contact damping force $\boldsymbol{F}_d^c$ is introduced to account for the energy dissipation when two spheres collide. The normal and tangential contact damping forces can be written as

$$F_{dn}^c = \beta_c \sqrt{2m_p K_n^c}\ v_n^c, \tag{2.7}$$

$$F_{dt}^c = \beta_c \sqrt{2m_p K_t^c}\ v_t^c, \tag{2.8}$$

in which m_p is the mass of a bonded particle or fibre. The symbols K_n^c and K_t^c represent the contact normal stiffness and the contact tangential stiffness respectively. The expressions of K_n^c and K_t^c are given by Thornton & Yin (1991) and also summarized in Guo (2010). The variables v_n^c and v_t^c represent the normal and tangential components respectively of the relative velocity at the contact point. In (2.6), $\boldsymbol{M}_d^c$ is the moment arising from the contact damping force $\boldsymbol{F}_d^c$.

Analogously to contact damping, bond damping is proposed to take into account the energy dissipation due to elastic wave propagation within a particle. Thus, the bond damping forces and moments are assumed to follow

$$F_{dn}^b = \beta_b \sqrt{2m_s K_n^b}\ v_n^r, \tag{2.9}$$

$$F_{dt}^b = \beta_b \sqrt{2m_s K_t^b}\ v_t^r, \tag{2.10}$$

https://doi.org/10.1017/jfm.2015.289 Published online by Cambridge University Press

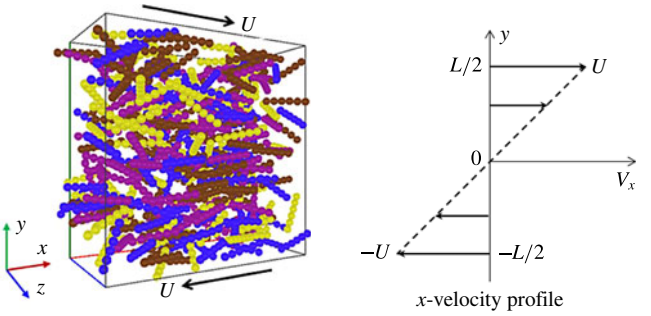


FIGURE 2. (Colour online) Numerical model of shear flow with flexible fibres (solid volume fraction = 0.1). The different coloured fibres are for identification purposes only.

$$M^b_{dn} = \beta_b \sqrt{2J_s K^b_{tor}}\,\omega^r_n, \tag{2.11}$$

$$M^b_{dt} = \beta_b \sqrt{2J_s K^b_{ben}}\,\omega^r_t. \tag{2.12}$$

The bond damping coefficient β_b varies in the range 0–1 and determines the energy dissipation rate. The bond damping force $\boldsymbol{F}^b_d$ and bond damping moment $\boldsymbol{M}^b_d$ (based on (2.9)–(2.12)) are added to (2.5) and (2.6).

2.2. *Computational set-up of shear flow*

As shown in figure 2, a specified number of fibres were generated in a shear cell, with the fibres randomly positioned and oriented. A procedure for the generation of a densely packed bed of elongated particles in a confined space is provided in Guo *et al.* (2012). Shear was initiated by applying a linear x-velocity (V_x) profile in the y direction with zero velocity at the centre,

$$V_x(y) = \gamma \cdot (y - y_c), \tag{2.13}$$

in which the applied shear strain rate γ can be expressed as $\gamma = 2U/L$, where L represents the distance between the top and bottom boundaries and U is the magnitude of the particle x-velocity at the top and bottom boundaries. In (2.13), y is the y coordinate of the mass centre of a fibre and y_c is the y coordinate of the centre of the shear cell. At the beginning of a simulation, each fibre has an initial x-velocity based on its mass centre y coordinate using (2.13). The initial translational velocities in the y and z directions and initial angular velocities are all set to zero for each fibre. Periodic boundary conditions were applied in the x and z directions, and a Lees–Edwards boundary condition (Lees & Edwards 1972) was adopted in the y direction. Shear flows were performed in the absence of gravity and an interstitial fluid. The volume of shear cell was fixed, and consequently the average solid volume fraction was fixed during the shear flow for a given number of fibres. In the present simulations, the measurement of quantities, such as stress, kinetic energy, potential energy (PE) and deforming parameter, is made when the shear flow reaches steady state. At steady state, these quantities remain approximately constant with limited fluctuations (Guo *et al.* 2012).

A shear cell with dimensions $[x, y, z]$ of $[15.12d_v, 15.12d_v, 7.56d_v]$, in which d_v is the equivalent sphere volume diameter of a fibre, was employed in this study. According to a shear cell size sensitivity test in our recent work (Guo *et al.* 2012),

https://doi.org/10.1017/jfm.2015.289 Published online by Cambridge University Press

reliable solid-phase stress results can be obtained at a relatively small computational cost using a shear cell of the same size for flows of rigid rod-like particles. The material and operating parameters used in the simulations are listed in table 1. Using a base case set of simulation conditions, the effects of bond stiffness, bond damping, interfibre friction, fibre aspect ratio and solid volume fraction on fibre flow behaviour have been explored.

3. Quantities associated with flexible fibres

In this section, the fibre mechanical energies, fibre deforming parameter and solid-phase stresses are introduced to quantitatively characterize individual fibre mechanical behaviour and bulk flow behaviour of a fibre system.

3.1. *Mechanical energies*

As external forces are applied to bulk materials, particles gain kinetic energy as they are propelled to translate and rotate. If the particles are flexible, significant PE can also be generated as they undergo large deformation. Meanwhile, these mechanical energies can be dissipated during particle collision and vibration processes. The kinetic energy of a fibre, E_{kin}, can be decomposed into global kinetic energy (GKE), E_{kin}^{glo}, and local kinetic energy (LKE), E_{kin}^{loc},

$$E_{kin} = E_{kin}^{glo} + E_{kin}^{loc}, \tag{3.1}$$

in which the GKE, E_{kin}^{glo}, is given by the total mass, m_p, and the translational velocity of the mass centre of the fibre (O), v_O, as

$$E_{kin}^{glo} = \tfrac{1}{2} m_p v_O^2. \tag{3.2}$$

The LKE, E_{kin}^{loc}, which describes the kinetic energy relative to the mass centre of the fibre, is given by

$$E_{kin}^{loc} = \frac{1}{2}\sum_{i=1}^{N_s} m_{si}(v_{si}^r)^2 + \frac{1}{2}\sum_{i=1}^{N_s} J_{si}(\omega_{si})^2, \tag{3.3}$$

in which N_s is the number of constituent spheres in the fibre, v_{si}^r is the relative velocity of the constituent sphere i of mass m_{si} to the centre of mass of the fibre, and J_{si} and ω_{si} are the moment of inertia and angular velocity (in the global frame of reference) respectively of the constituent sphere i. Based on (3.2) and (3.3), the GKE is caused by the translation of the fibre and the LKE is generated by the rotation and vibration of the fibre.

Elastic PE, E_{pot}, is generated due to the elastic deformation of bonds and can be expressed as

$$E_{pot} = \sum_{i=1}^{N_b}\left[\frac{1}{2}\frac{E_b A}{l_b}(\delta_{ni}^b)^2 + \frac{1}{2}\frac{G_b A}{l_b}(\delta_{ti}^b)^2 + \frac{1}{2}\frac{G_b I_p}{l_b}(\theta_{ni}^b)^2 + \frac{1}{2}\frac{E_b I}{l_b}(\theta_{ti}^b)^2\right], \tag{3.4}$$

in which N_b is the number of bonds in a fibre. In addition, δ_{ni}^b, δ_{ti}^b, θ_{ni}^b and θ_{ti}^b represent the current normal deformation, shear deformation, torsional angular deformation and bending angular deformation respectively of the bond i.

https://doi.org/10.1017/jfm.2015.289 Published online by Cambridge University Press

https://doi.org/10.1017/jfm.2015.289 Published online by Cambridge University Press

	Fibre properties										Operating parameters	
	E_b (Pa)	β_b	ζ_b	d_v (μm)	E_s (Pa)	ρ_s (kg m^{-3})	ζ_s	β_c	μ	AR	γ (s^{-1})	Solid volume fraction (v)
Base case values	2.6×10^4	0.0	0.3	476.2	8.7×10^7	2.5×10^3	0.3	1.63×10^{-2}	0.0	6	100	0.1
Other values used	2.6×10^2	3.99×10^{-4}	N/A	N/A	N/A	N/A	N/A	N/A	0.125	2	N/A	0.025, 0.05
	2.6×10^6	4.01×10^{-3}							0.25	4		0.2
	1.0×10^8	4.2×10^{-2}							0.375	8		0.3
		0.114							0.5			0.4
		0.267							0.75			0.4663
		0.676										

TABLE 1. Material properties and operating parameters used in the simulations. AR, fibre aspect ratio.

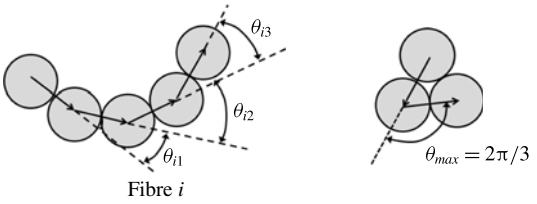


FIGURE 3. Illustration for the definition of the fibre deforming parameter.

3.2. *Deforming parameter*

A fibre can experience bending, twisting and axial stretching deformations, among which the bending deformation may be the most significant for elongated fibres. In order to quantify the extent of the bending deformation of a fibre i, a deforming parameter S_i is defined as

$$S_i = \frac{1}{\theta_{max}} \sqrt{\frac{1}{K} \sum_{j=1}^{K} \theta_{ij}^2}, \tag{3.5}$$

in which θ_{ij} is the angle between two neighbouring bonds (separated by a length of one sphere diameter) and K is the number of angles θ_{ij} in the fibre i. As illustrated in figure 3, the maximum angle θ_{max} between such two bonds is equal to $2\pi/3$. For a system of N fibres, the mean value of the deforming parameters of all the fibres, S_{mean}, can be used to characterize the extent of fibre deformation for the system,

$$S_{mean} = \frac{1}{N} \sum_{i=1}^{N} S_i. \tag{3.6}$$

The mean deforming parameter S_{mean} varies in the range [0, 1], and a larger value of S_{mean} indicates larger average bending deformation of fibres.

3.3. *Solid-phase stress*

The solid-phase stress tensor of a bulk system can be expressed as the sum of a kinetic or streaming component and a collisional component. Following Campbell & Gong (1986), the kinetic component, which arises from momentum transfer by fibres as they move through the bulk material, is given by

$$\boldsymbol{\sigma}_{kin} = \rho v \langle \boldsymbol{C} \otimes \boldsymbol{C} \rangle, \tag{3.7}$$

in which $\langle\,\rangle$ represents an average over time and volume, and $\boldsymbol{C} = \boldsymbol{c}_i - \langle \boldsymbol{c} \rangle$ is the fluctuating velocity of fibre i. The average velocity $\langle \boldsymbol{c} \rangle$ is the local steady-state shear velocity (i.e. the average velocity in the shear layer where fibre i resides). The collisional component, which arises from momentum transfer from one point to another in the material by interparticle collisions, is written as

$$\boldsymbol{\sigma}_{col} = \langle \boldsymbol{F}_i^j \otimes \boldsymbol{l}_{ic} + \boldsymbol{F}_j^i \otimes \boldsymbol{l}_{jc} \rangle, \tag{3.8}$$

where $\boldsymbol{F}_i^j$ is the contact force exerted on fibre i by fibre j, and $\boldsymbol{l}_{ic}$ is the vector pointing from the mass centre of fibre i to the contact point. Similarly, $\boldsymbol{F}_j^i$ is the contact force

https://doi.org/10.1017/jfm.2015.289 Published online by Cambridge University Press

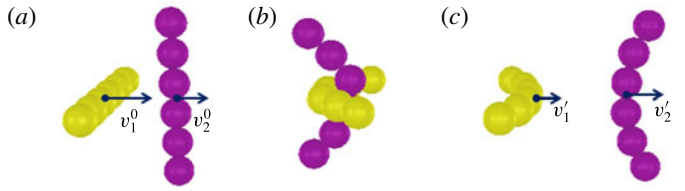


FIGURE 4. (Colour online) Snapshots from a collinear collision between two flexible fibres arranged with their two major axes perpendicular to each other. An initial velocity is given to the fibre on the left-hand side: (*a*) before collision, (*b*) during collision, (*c*) after collision.

exerted on fibre j by fibre i, and $\boldsymbol{l}_{jc}$ is the vector pointing from the mass centre of fibre j to the contact point. For contact between fibres i and j, according to Newton's third law, $\boldsymbol{F}_j^i = -\boldsymbol{F}_i^j$, so that (3.8) can be rewritten as

$$\boldsymbol{\sigma}_{col} = \langle \boldsymbol{F}_i^j \otimes (\boldsymbol{l}_{ic} - \boldsymbol{l}_{jc}) \rangle = \langle \boldsymbol{F}_i^j \otimes \boldsymbol{l}_{ij} \rangle, \tag{3.9}$$

in which $\boldsymbol{l}_{ij}$ represents the vector from the mass centre of fibre i to the mass centre of fibre j. In this study, the measurements of fibre system stresses are made by calculating (3.7) and (3.9) and summing them.

4. Collinear collision between two fibres

In order to understand the mechanical response of fibres during and after a contact, collinear collision between two fibres, which are perpendicular to each other, is modelled as illustrated in figure 4. The initial velocity of fibre 1 is set to v_1^0, with the direction from the centre of fibre 1 to the centre of fibre 2, and fibre 2 has a zero initial velocity, i.e. $v_2^0 = 0$. Figure 5 shows the evolution of various mechanical energies before, during and after the collision of two flexible fibres, in which E represents the average GKE, average LKE or average bond PE per fibre, and E_{tot}^0 is the initial average total mechanical energy (TME) per fibre. At the beginning of the collision, the GKE is converted to LKE and the bond PE as the fibres deform. Before two fibres bounce off each other, the LKE and the bond PE are partially converted back to GKE, leading to an increase in the GKE at the end of the collision. After collision, the GKE remains constant, while the LKE and bond PE oscillate as the fibres vibrate. Without bond damping (i.e. $\beta_b = 0$), as shown in figure 5(*a–c*), the LKE and bond PE fluctuate around a constant level. It is also observed that a smaller extent of fluctuation is obtained with a larger bond Young's modulus E_b. With bond damping (i.e. $\beta_b = 0.676$), as shown in figure 5(*d–f*), the LKE and bond PE decrease with time as the fibre vibration decays. Quicker damping of energies is observed with a larger bond Young's modulus due to the higher vibration frequency.

The effective coefficient of restitution is defined as the ratio of postcollisional relative velocity to precollisional relative velocity of the mass centres of two fibres for a collinear collision, as shown in figure 4,

$$e = \frac{v_2' - v_1'}{v_1^0 - v_2^0} = \frac{v_2' - v_1'}{v_1^0}. \tag{4.1}$$

Conservation of linear momentum leads to

$$m_p v_1^0 = m_p v_1' + m_p v_2'. \tag{4.2}$$

https://doi.org/10.1017/jfm.2015.289 Published online by Cambridge University Press

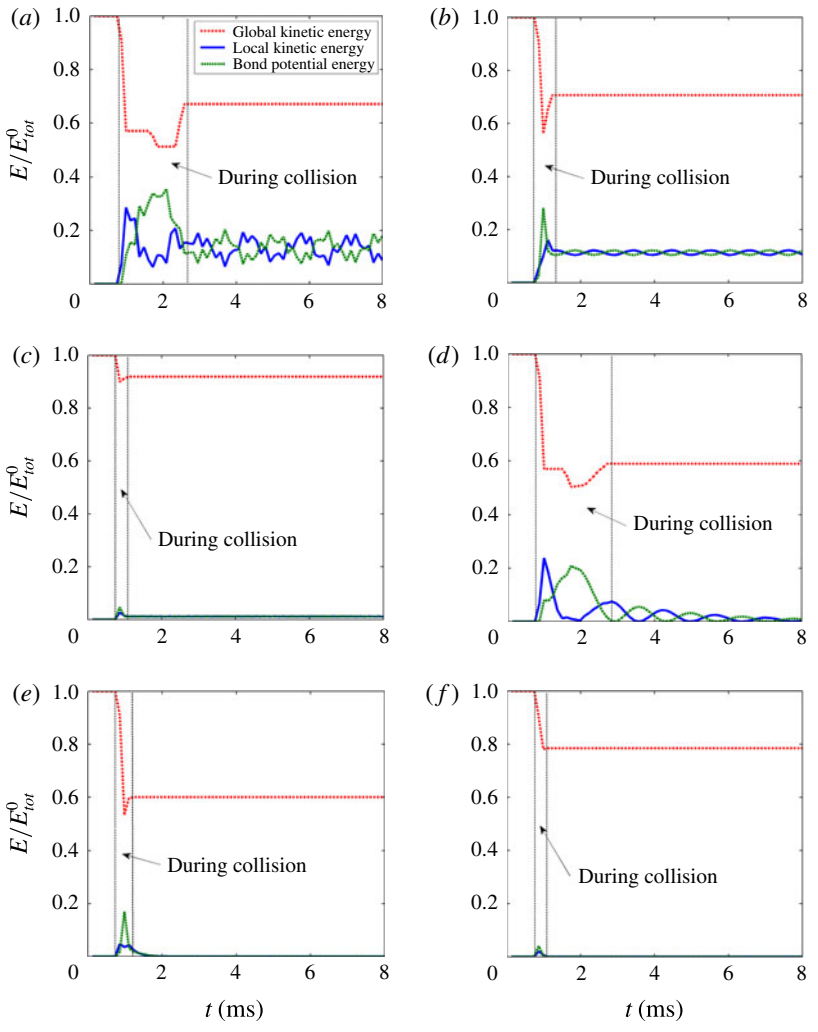


FIGURE 5. (Colour online) The evolution of various mechanical energies before, during and after the collision of two flexible fibres ($\mu = 0$, $\beta_c = 1.63 \times 10^{-2}$, $AR = 6$): (*a*) $E_b = 2.6 \times 10^4$ Pa, $\beta_b = 0$; (*b*) $E_b = 2.6 \times 10^6$ Pa, $\beta_b = 0$; (*c*) $E_b = 1.0 \times 10^8$ Pa, $\beta_b = 0$; (*d*) $E_b = 2.6 \times 10^4$ Pa, $\beta_b = 0.676$; (*e*) $E_b = 2.6 \times 10^6$ Pa, $\beta_b = 0.676$; (*f*) $E_b = 1.0 \times 10^8$ Pa, $\beta_b = 0.676$.

From (4.1) and (4.2), we obtain

$$v_1' = \tfrac{1}{2}(1 - e)v_1^0 \tag{4.3}$$

and

$$v_2' = \tfrac{1}{2}(1 + e)v_1^0. \tag{4.4}$$

The precollisional GKE of two fibres is expressed by

$$(E_{kin}^{glo})^{pre} = \tfrac{1}{2}m_p(v_1^0)^2 \tag{4.5}$$

https://doi.org/10.1017/jfm.2015.289 Published online by Cambridge University Press

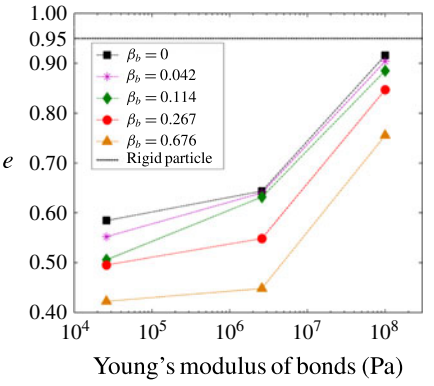


FIGURE 6. (Colour online) Effective coefficients of restitution at various bond Young's moduli and bond damping coefficients ($\mu = 0$, $\beta_c = 1.63 \times 10^{-2}$, $AR = 6$).

and the postcollisional GKE is

$$(E_{kin}^{glo})^{pos} = \tfrac{1}{2} m_p (v_1')^2 + \tfrac{1}{2} m_p (v_2')^2. \tag{4.6}$$

By substituting (4.3)–(4.5), we have

$$(E_{kin}^{glo})^{pos} = \tfrac{1}{2}(1 + e^2)(E_{kin}^{glo})^{pre}. \tag{4.7}$$

Therefore, the effective coefficient of restitution, e, can be expressed as

$$e = \sqrt{\frac{2(E_{kin}^{glo})^{pos}}{(E_{kin}^{glo})^{pre}} - 1}. \tag{4.8}$$

If there is no reduction in the total GKE, i.e. $(E_{kin}^{glo})^{pos} = (E_{kin}^{glo})^{pre}$, e is equal to one. As the postcollisional GKE, $(E_{kin}^{glo})^{pos}$, decreases, e decreases. A zero effective coefficient of restitution ($e = 0$) is obtained when v_2' is equal to v_1', since $(E_{kin}^{glo})^{pos}$ is equal to half of $(E_{kin}^{glo})^{pre}$.

Figure 6 shows the effective coefficients of restitution with various bond Young's moduli and bond damping coefficients. A contact damping coefficient of $\beta_c = 1.63 \times 10^{-2}$, which leads to an effective coefficient of restitution of 0.95 for the collinear collision of two rigid fibres, is employed in all the simulations. In general, the effective coefficients of restitution of flexible fibres are smaller than that of a rigid fibre (i.e. 0.95) due to a reduction in GKE after a collision caused by the fact that part of the GKE is converted to PE and LKE for contacting flexible fibres. It can be seen that the effective coefficient of restitution increases as the bond Young's modulus increases, and decreases as the bond damping coefficient increases. As the bond stiffness increases, the collision duration decreases and more GKE remains after the collision (see figure 5), leading to a higher effective coefficient of restitution. The bond damping dissipates the LKE; therefore, less GKE remains after the collision due to conversion to LKE, which is dissipated in the damped bonds. As a result, the effective coefficient of restitution is reduced with an increase in bond damping.

https://doi.org/10.1017/jfm.2015.289 Published online by Cambridge University Press

5. Shear flows of flexible fibres

Granular shear flows are commonly encountered in industrial solids handling processes, such as feeding, discharging, conveying and blending. An understanding of the mechanisms that control the flow behaviour is essential for the design and optimization of handling systems. Using the DEM-based flexible fibre model, simulations of shear flows of flexible fibres with and without friction have been performed. The effects of fibre properties, such as stiffness, damping, friction, surface roughness and aspect ratio, on fibre deformation, orientation, mechanical energies and bulk phase stresses at various solid volume fractions are comprehensively discussed in this section.

5.1. *Frictionless fibres*

Fibre alignment and deformation

Fibre deformation has a significant impact on the microstructure of a fibre system. The studies in § 4 show that fibre deformation strongly depends on the bond stiffness and bond damping for a collinear collision, as shown in figure 4. The effect of solid volume fraction on the extent of fibre deformation in shear flows is investigated in this section, and the effect of interfibre friction is discussed in § 5.2.

Snapshots of shear flows of frictionless flexible fibres at low, intermediate and high solid volume fractions ($v = 0.05$, 0.3 and 0.466) are shown in figure 7. In a dilute flow with a solid volume fraction of $v = 0.05$, significant fibre bending deformation and vibration are observed after collisions. As the solid volume fraction increases, the deformation of fibres becomes very limited, and the elongated fibres tend to align. For the roughly straight fibres, one may define the line connecting two spheres at each end of a bonded-sphere fibre as the major axis of the fibre. Then, the orientation of an approximately straight fibre can be described using two angles: α, the angle between the major axis of the fibre and the horizontal plane (x–z plane), and ϕ, the angle between the projection of the major axis on the x–z plane and the x-axis, as illustrated in figure 8(a). The probability density functions of the fibre orientation in terms of α and ϕ are shown in figures 8(b) and 8(c) respectively. In figure 8(b), it is evident that both flexible and rigid fibres tend to align with a small positive angle (approximately 6.5°) from the shear plane (i.e. x–z plane). This alignment phenomenon is similar to previous observations (Reddy, Kumaran & Talbot 2009; Campbell 2011; Börzsönyi *et al.* 2012*a*,*b*; Guo *et al.* 2013*a*; Hua *et al.* 2013). As shown in figure 8(c), a narrow symmetric probability density function of ϕ is obtained with the peak value at approximately $\phi = 0°$, indicating that the projections of the major axes of the fibres on the x–z plane tend to align within a small positive or negative angle from the flow direction (i.e. x direction).

The variation of the deforming parameter (S_{mean}) with the solid volume fraction (v) for the frictionless fibres with and without bond damping (β_b) is plotted in figure 9. Without bond damping ($\beta_b = 0$), the deforming parameter generally decreases with increasing solid volume fraction. This trend may be attributed to the alignment of fibres at high solid volume fractions, as shown in figure 7. At low solid volume fractions, fibre bending deformation is promoted as two fibres contact with a significant angle between long axes. However, at high solid volume fractions, the alignment of fibres leads to the dominance of end–end contact, for which one end of a fibre touches the end of another fibre, and parallel contact, for which the long axes of two contacting fibres are nearly parallel to each other. The bending deformation

https://doi.org/10.1017/jfm.2015.289 Published online by Cambridge University Press

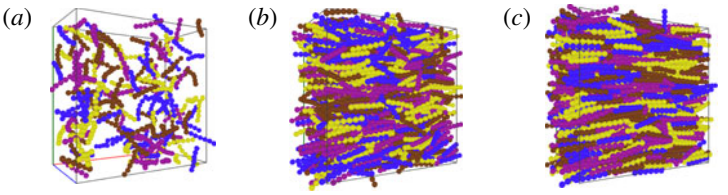


FIGURE 7. (Colour online) Snapshots from shear flows of frictionless flexible fibres at low, intermediate and high solid volume fractions v ($\mu = 0$, $\beta_c = 1.63 \times 10^{-2}$, $\beta_b = 0$, $E_b = 2.6 \times 10^4$ Pa, $AR = 6$). The different coloured fibres are for identification purposes only: (*a*) $v = 0.05$, (*b*) $v = 0.3$, (*c*) $v = 0.466$.

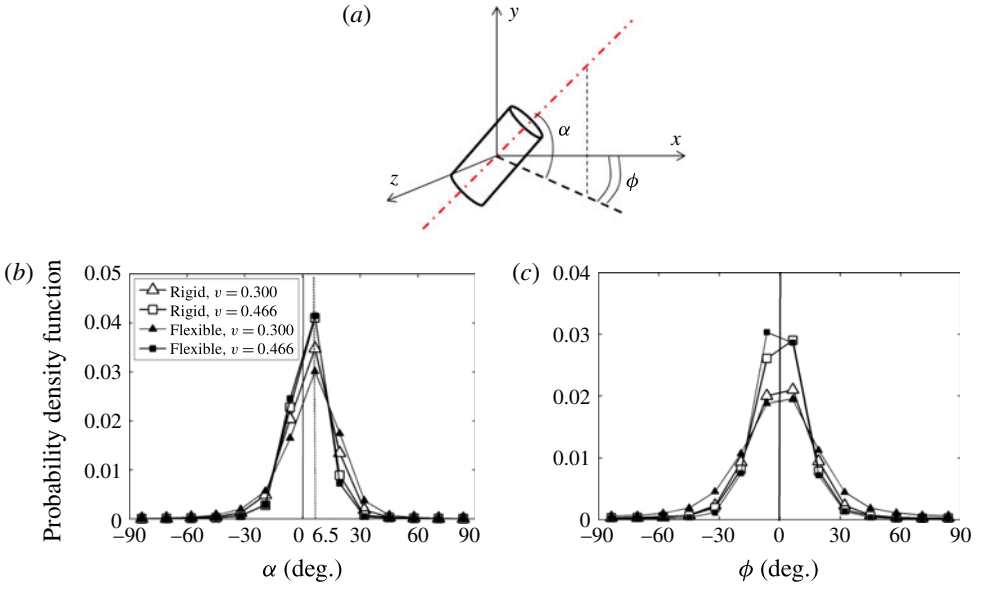


FIGURE 8. (Colour online) (*a*) Description of elongated particle orientation using α, the angle between the major axis of the particle and the horizontal plane (x–z plane), and ϕ, the angle between the projection of the major axis on the x–z plane and the x-axis. (*b,c*) Probability density function of the fibre orientation in terms of the angle α and the angle ϕ respectively. The flexible fibres have the properties $\mu = 0$, $\beta_c = 1.63 \times 10^{-2}$, $\beta_b = 0$, $E_b = 2.6 \times 10^4$ Pa, $AR = 6$.

of fibres is prohibited by end–end contact and parallel contact. As a result, the deformation of frictionless fibres is reduced due to the fibre alignment as the solid volume fraction increases.

As discussed in § 4, in the presence of bond damping, the vibration of fibres decays and the fibre shape can quickly recover after collisions. As a result, smaller deforming parameters are obtained with bond damping ($\beta_b = 4.2 \times 10^{-2}$) compared with those without bond damping ($\beta_b = 0$), as shown in figure 9. However, an increase in the deforming parameter at high solid volume fractions is observed with bond damping. The collision frequency increases and the time between two consecutive collisions decreases as the solid volume fraction increases. Thus, the time for a vibrating fibre to recover its shape due to bond damping can be longer than the time between two

https://doi.org/10.1017/jfm.2015.289 Published online by Cambridge University Press

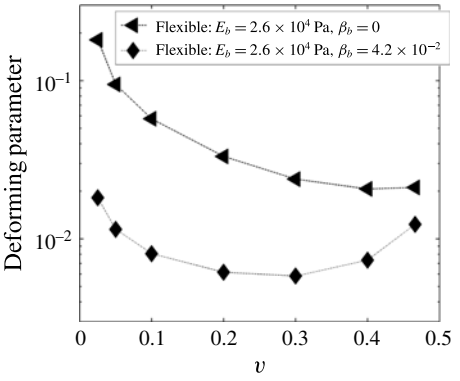


FIGURE 9. Deforming parameter as a function of solid volume fraction with and without bond damping ($\mu = 0$, $\beta_c = 1.63 \times 10^{-2}$, $E_b = 2.6 \times 10^4$ Pa, $AR = 6$).

consecutive collisions at high solid volume fractions. As a result, the effect of bond damping on the fibre deformation and vibration is reduced at high solid volume fractions, due to the fact that the time duration between two consecutive collisions is too short for a fibre to recover its shape via bond damping.

Fibre mechanical energies

As discussed previously, kinetic energy reflects translational motion, rotational motion and vibration of fibres, and PE is associated with fibre deformation (see § 3.1). In addition, the conversion between kinetic and potential energies and the energy dissipation have a significant impact on the effective coefficient of restitution for a collision between two fibres (see § 4). Hence, the fibre mechanical energies may provide an important perspective for understanding particle motion, deformation and interaction. As a result, the effects of fibre flexibility, bond damping and solid volume fraction on different forms of mechanical energy, including local and global kinetic energies and PE, are examined in this section.

The average elastic PE, LKE, GKE and TME per fibre, normalized by $m_p d_v^2 \gamma^2$, are plotted as a function of solid volume fraction for shear flows of rigid and flexible fibres in figure 10(*a–d*). The elastic energy, LKE and GKE are defined in § 3.1, and the TME is the sum of these three energies. Due to the fact that the elastic energy due to particle deformation does not exist for the rigid fibres, the normalized average elastic energies per fibre ($E_{pot}/(m_p d_v^2 \gamma^2)$) are plotted only for the flexible fibres in figure 10(*a*). Bond damping leads to a reduction in fibre vibration and consequently dissipation of elastic energy, as shown in figure 5(*d*). As a result, smaller elastic energy is obtained for flexible fibres with bond damping compared with those without bond damping. The average elastic energy per fibre without bond damping generally decreases with increasing solid volume fraction, while the average elastic energy per fibre with bond damping initially decreases and then increases with increasing solid volume fraction. These trends in elastic energy are similar to those of the deforming parameter (figure 9). This behaviour is not surprising considering that the elastic energy is determined by the bond deformation, as described in (3.4).

The LKE represents the kinetic energy caused by the rotation and vibration of the fibre (see § 3.1). The flexible fibres can rotate and vibrate, while the rigid fibres only rotate and do not vibrate. As a result, the flexible fibres without bond damping, which vibrate vigorously, can have larger average LKEs than the rigid fibres, as shown in

https://doi.org/10.1017/jfm.2015.289 Published online by Cambridge University Press

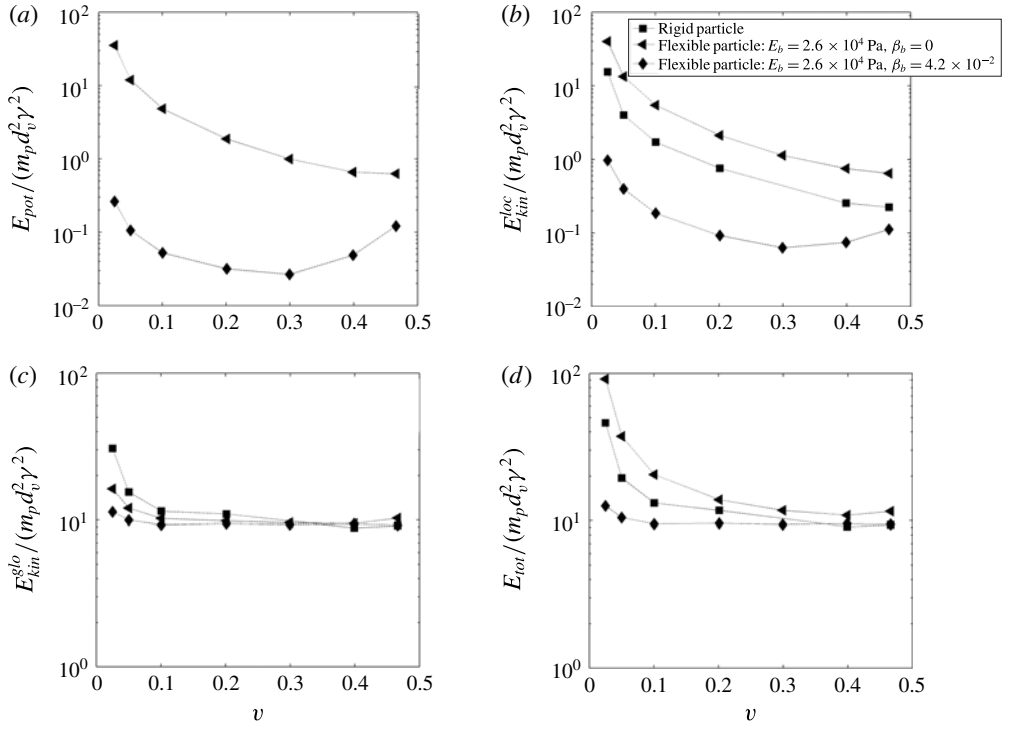


FIGURE 10. Average mechanical energies per fibre as a function of solid volume fraction for shear flows of rigid and flexible fibres ($\mu = 0$, $\beta_c = 1.63 \times 10^{-2}$, $AR = 6$): (*a*) elastic potential energy (PE), (*b*) local kinetic energy (LKE), (*c*) global kinetic energy (GKE), (*d*) total mechanical energy (TME).

figure 10(*b*). However, when bond damping is introduced to the flexible fibres, the LKE, like elastic energy, can also be damped rapidly during vibration (see figure 5*d*). Thus, the flexible fibres with bond damping have smaller average LKEs than both the flexible fibres without bond damping and the rigid fibres.

The GKE is determined by the translational velocity of a fibre (3.2). For dilute systems, transient and binary collisions are dominant. After a binary collision, the GKE is proportional to $(1 + e^2)$ according to (4.7). Since the effective coefficient of restitution e decreases as follows: rigid particle $>$ flexible particle without bond damping $>$ flexible particle with bond damping (figure 6), the same rank ordering is obtained for the GKE in dilute systems ($v < 0.2$; figure 10*c*). For dense granular systems, enduring and multiple interparticle contacts become dominant, and the motion of a fibre, which is constrained by neighbouring fibres, follows the local mean flow. Thus, the translational velocities of fibres are determined mainly by the specified linear velocity profile and shear rate. As a result, the GKEs remain nearly the same for the rigid fibres and flexible fibres with and without bond damping at solid volume fractions greater than 0.2.

The average TME per fibre, which is the sum of the average elastic energy, LKE and GKE per fibre, is plotted in figure 10(*d*). In dilute systems ($v < 0.2$), the average TME decreases sharply with increasing solid volume fraction. Flexible fibres without bond damping have greater average TMEs than rigid fibres due to the large elastic energy and large LKE. Flexible fibres with bond damping can have smaller average

https://doi.org/10.1017/jfm.2015.289 Published online by Cambridge University Press

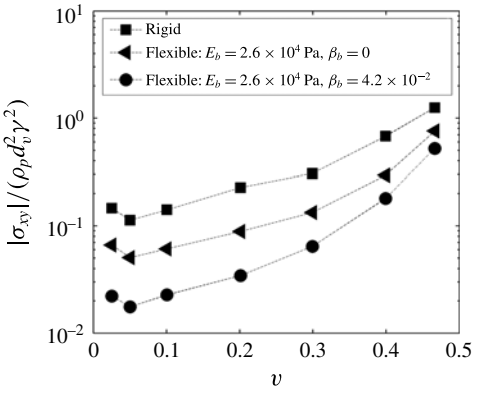


FIGURE 11. Normalized shear stress as a function of solid volume fraction for shear flows of rigid and flexible fibres ($\mu = 0$, $\beta_c = 1.63 \times 10^{-2}$, $AR = 6$).

TMEs than rigid fibres since the elastic energy, LKE and GKE could all be reduced by the bond damping. In dense systems ($\upsilon > 0.2$), the average TME changes slightly with increasing solid volume fraction, and the average TMEs of flexible fibres without bond damping are slightly larger than those of rigid fibres and flexible fibres with bond damping. At large solid volume fractions ($\upsilon > 0.2$), the nearly constant TME is attributed to the dominance of GKEs, which are at least one order of magnitude larger than the elastic energies and LKEs.

Bulk stresses

The stresses of bulk materials are required to determine constitutive relations for granular flows. Hence, the effects of fibre flexibility and bond damping on the stresses are also explored in the present work. Figure 11 shows the shear stress, normalized by $\rho_p d_v^2 \gamma^2$, as a function of solid volume fraction for shear flows of rigid fibres and flexible fibres with and without bond damping. Similar trends are observed for both the rigid and the flexible fibres. As the solid volume fraction increases, the normalized shear stress initially decreases due to the reduction in mean free path (leading to a reduction in velocity fluctuations) and then increases due to the increase in collision frequency. Compared with rigid fibres, smaller stresses are obtained for flexible fibres without bond damping, and even smaller stresses are obtained with bond damping. One of the major reasons for the stress difference between the rigid fibres and flexible fibres is due to the difference in the effective coefficient of restitution e. As shown in figure 6, the effective coefficients of restitution e of the flexible fibres without bond damping are smaller than that of the rigid fibres due to the conversion of part of the kinetic energy to PE. In addition, even smaller e values are obtained for the flexible fibres with bond damping due to energy dissipation in the vibration of fibres. According to granular kinetic theory for spherical particles (Lun *et al.* 1984), the granular temperature T is proportional to $1/(1-e^2)$, the shear stress σ_{xy} is proportional to $\sqrt{T}$ and the normal stress σ_{yy} is proportional to T. Therefore, smaller effective coefficients of restitution e lead to lower granular temperatures, and consequently smaller stresses. In addition, compared with the rigid particles, the deformation of flexible fibres allows the fibres to be rearranged in a more restrictive space and therefore smaller contact forces are obtained.

The apparent friction coefficient, defined as the ratio of shear to normal stress magnitudes ($|\sigma_{xy}|/\sigma_{yy}$), is plotted as a function of solid volume fraction in figure 12.

https://doi.org/10.1017/jfm.2015.289 Published online by Cambridge University Press

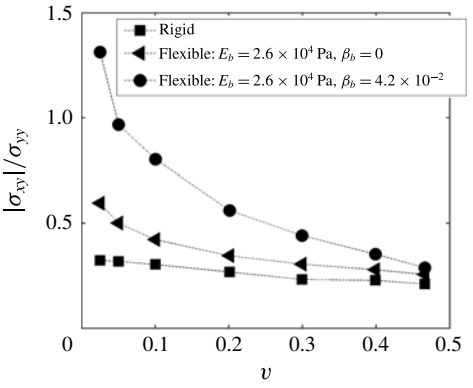


FIGURE 12. The apparent friction coefficient as a function of solid volume fraction for rigid and flexible fibres without friction ($\mu = 0$, $\beta_c = 1.63 \times 10^{-2}$, $AR = 6$).

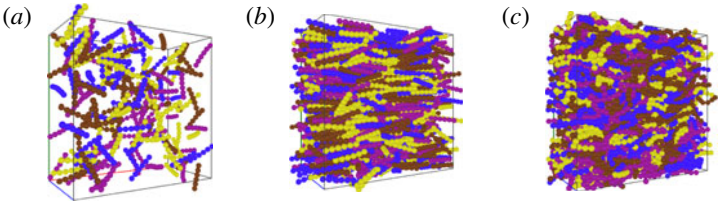


FIGURE 13. (Colour online) Snapshots from shear flows of flexible fibres with a friction coefficient of $\mu = 0.5$ at various solid volume fractions ($\beta_c = 1.63 \times 10^{-2}$, $E_b = 2.6 \times 10^4$ Pa, $\beta_b = 0$, $AR = 6$). The different coloured fibres are for identification purposes only: (*a*) $v = 0.05$, (*b*) $v = 0.3$, (*c*) $v = 0.466$.

Granular kinetic theory predicts that the apparent friction coefficient, $|\sigma_{xy}|/\sigma_{yy}$, is proportional to $1/\sqrt{T}$. Thus, as the effective coefficient of restitution e decreases, the granular temperature T decreases, leading to an increase in the apparent friction coefficient. As a result, larger apparent friction coefficients are observed for flexible fibres, particularly with bond damping, compared with rigid fibres. In general, the apparent friction coefficient decreases with increasing solid volume fraction, as the fibres tend to align and move in horizontal layers (see figure 7). However, a much steeper decrease is observed for the flexible fibres with bond damping, and the apparent friction coefficients of rigid and flexible fibres tend to converge at large solid volume fractions. These observations indicate that the fibre flexibility and bond damping have a smaller impact on the apparent friction coefficient in dense flows than in dilute flows.

According to (1.1), the normalized normal stress σ_{yy} (i.e. pressure P) can be correlated with the inertial number I as follows:

$$\frac{\sigma_{yy}}{\rho_p d_v^2 \gamma^2} = \frac{1}{I^2}. \tag{5.1}$$

Therefore, the solid volume fraction and bulk friction coefficient can also be expressed as a function of the inertial number.

https://doi.org/10.1017/jfm.2015.289 Published online by Cambridge University Press

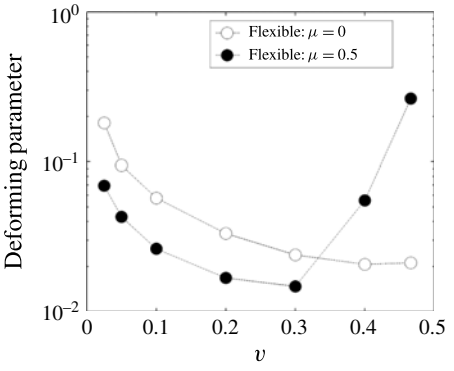


FIGURE 14. Effect of friction on fibre deformation ($\beta_c = 1.63 \times 10^{-2}$, $E_b = 2.6 \times 10^4$ Pa, $\beta_b = 0$, $AR = 6$).

5.2. *Effect of interfibre friction*

Previous studies of rigid rod-like particles (Guo *et al.* 2013*a*) indicate that interparticle friction has a significant effect on the particle flow pattern and solid-phase stresses. Subsequently, it is interesting to examine the effect of friction on flexible fibre flows. Snapshots of shear flows of flexible fibres with an interfibre friction of $\mu = 0.5$ at various solid volume fractions are shown in figure 13. At an intermediate solid volume fraction ($v = 0.3$), the fibres with friction tend to align with a small angle from the flow direction, as observed for frictionless fibres (figure 7*b*). However, large fibre deformation is observed at the high solid volume fraction of $v = 0.466$ (see figure 13*c*) due to the fact that the frictional forces can cause strong contacts and large fibre bending. A comparison of deforming parameters with and without friction is made in figure 14. The deforming parameter decreases monotonically with increasing solid volume fraction for the frictionless flexible fibres, while a U-shaped trend is observed for the flexible fibres with friction. At small solid volume fractions ($v < 0.3$), smaller deforming parameters are obtained with friction than without friction, due to the dissipation of kinetic energy by sliding friction. However, at large solid volume fractions ($v > 0.3$), larger deforming parameters are obtained with friction compared with the without friction case, which is consistent with the observations of fibre deformation in figures 7(*c*) and 13(*c*).

The average elastic PE, LKE, GKE and TME per fibre, normalized by $m_p d_v^2 \gamma^2$, are plotted as a function of solid volume fraction for shear flows of rigid and flexible fibres with and without friction in figure 15. Since the rigid fibres have no elastic energies, only the elastic energies of flexible fibres are plotted in figure 15(*a*). Similarly to the deforming parameter (figure 14), the elastic energy also shows a U-shaped trend with increasing solid volume fraction for the flexible fibres with friction. The similarity reflects the dependence of the elastic energy on the fibre deformation. U-shaped trends are also observed for the LKEs of rigid and flexible fibres with friction, as shown in figure 15(*b*). For the flexible fibres with friction, the increased number of contacts at large solid volume fractions leads to larger fibre deformation, larger PE and stronger fibre vibration. For rigid fibres with friction, the increased number of contacts at large solid volume fractions can increase the rotation of fibres, causing the increase in the LKE. The average GKEs of rigid and flexible fibres with and without friction are plotted in figure 15(*c*). It can be seen that the

https://doi.org/10.1017/jfm.2015.289 Published online by Cambridge University Press

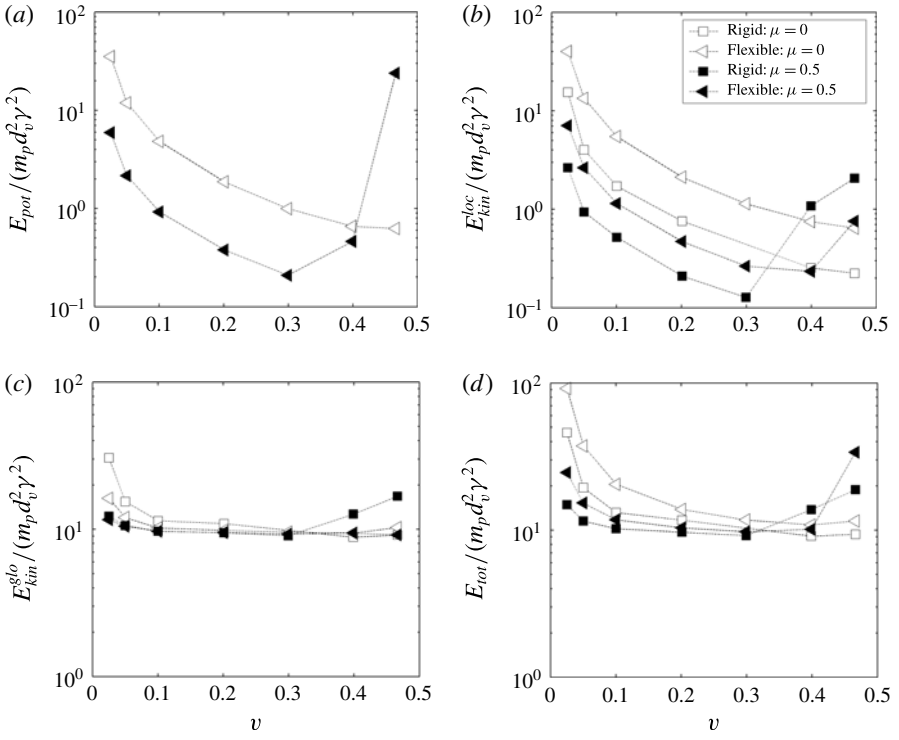


FIGURE 15. The average mechanical energies per fibre as a function of solid volume fraction for shear flows of rigid and flexible fibres with and without friction ($\beta_c = 1.63 \times 10^{-2}$, $E_b = 2.6 \times 10^4$ Pa, $\beta_b = 0$, $AR = 6$): (*a*) elastic potential energy (PE), (*b*) local kinetic energy (LKE), (*c*) global kinetic energy (GKE), (*d*) total mechanical energy (TME).

interfibre friction leads to smaller GKEs at small solid volume fractions ($v < 0.1$), due to the dissipation of kinetic energy through sliding friction. In dense flows of rigid fibres with friction, the fibres have a good chance of interlocking and forming agglomerates that possess large contact forces under the combined effects of high fibre stiffness and large friction. The shear-induced breakup of fibre agglomerates can result in high fibre velocities. As a result, large GKEs are obtained for the rigid fibres with friction at large solid volume fractions ($v > 0.3$). The average TMEs are plotted in figure 15(*d*). At small solid volume fractions ($v < 0.2$), smaller TMEs are obtained for the fibres with friction compared with the without friction case due to the fact that the friction can cause a reduction in the elastic energy, LKE and GKE in dilute flows. At large solid volume fractions, large TMEs are obtained for the fibres with friction. The large TME of rigid fibres with friction is mainly due to the large GKE caused by the strong contacts of fibres (figure 15*c*), while the large TME of flexible fibres with friction is primarily attributed to the large elastic energy induced by the large fibre deformation (figure 15*a*).

The variation of normalized shear stress with solid volume fraction for shear flows of rigid and flexible fibres with and without friction is plotted in figure 16. The insets show the networks of force chains for the frictionless and frictional flexible fibres at a solid volume fraction of $v = 0.466$. A force chain is plotted by connecting the

https://doi.org/10.1017/jfm.2015.289 Published online by Cambridge University Press

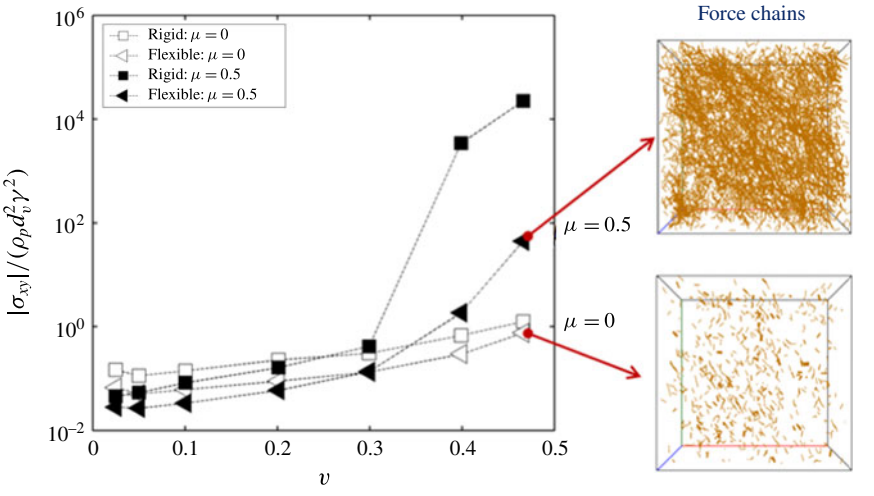


FIGURE 16. (Colour online) The normalized shear stress as a function of solid volume fraction in shear flows of rigid and flexible fibres with and without friction ($\beta_c = 1.63 \times 10^{-2}$, $E_b = 2.6 \times 10^4$ Pa, $\beta_b = 0$, $AR = 6$).

centres of two contacting constituent spheres from different fibres using a line, and the thickness of the line is scaled by the magnitude of the contact force. The effect of friction on the stress (figure 16) is similar to the effect of friction on the mechanical energies (figure 15). Compared with the fibres without friction, smaller stresses are obtained at small solid volume fractions and much larger stresses are observed at large solid volume fractions for the fibres with friction. At small solid volume fractions, the kinetic stress, which is determined by the fluctuating velocities, dominates the total stress. The reduction in GKE due to sliding friction (figure 15*c*) leads to a decrease in the fluctuating velocities and consequently the kinetic stresses. At large solid volume fractions, the enhanced interfibre contacts, as indicated by the dense network of force chains, lead to larger stresses for the frictional fibres. In addition, a less pronounced stress increase at high solid volume fractions is observed for the frictional flexible fibres than the frictional rigid fibres. The apparent friction coefficients of the rigid and flexible fibres with and without friction are plotted in figure 17. Similarly to the rigid fibres, interfibre friction leads to a significant increase in apparent friction coefficient for the flexible fibres. In addition, the apparent friction coefficient decreases as the solid volume fraction increases.

5.3. *Jamming in dense flows*

In frictional fibre flows at high solid volume fractions, long lasting, dense and system spanning force chains are formed to strongly resist the flow, causing a sharp stress increase (see figure 16). This fluid-like to solid-like phase transition phenomenon is defined as jamming. The dependence of the jamming onset on the interfibre friction, fibre surface roughness, bond Young's modulus (or stiffness) and fibre aspect ratio is explored in this section.

Figure 18 shows the normalized shear stress, coordination number and apparent friction coefficient as a function of interfibre friction coefficient μ for dense shear flows with $v = 0.466$. The coordination number is defined as the average number

https://doi.org/10.1017/jfm.2015.289 Published online by Cambridge University Press

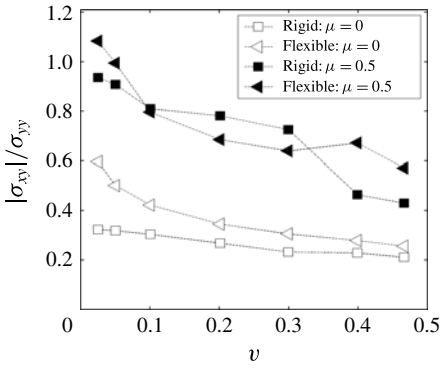


FIGURE 17. The apparent friction coefficient as a function of solid volume fraction for rigid and flexible fibres with and without friction ($\beta_c = 1.63 \times 10^{-2}$, $E_b = 2.6 \times 10^4$ Pa, $\beta_b = 0$, $AR = 6$).

of contacting neighbours per fibre, i.e. $(\sum_{i=1}^{N} N_i^n)/N$, in which N_i^n is the number of neighbouring fibres in contact with the fibre i and N is the total number of fibres in the system. Two types of fibre with the same aspect ratio of $AR = 6$ have been considered: (i) a rough fibre, which is formed by gluing six identical spheres in a line with the distance between two neighbouring spheres equal to the diameter of the sphere (no sphere–sphere overlap), and (ii) a smoothed fibre, which is formed by gluing eleven identical spheres in a line with the distance between two neighbouring sphere centres equal to the radius of the sphere (allowing sphere–sphere overlaps). For rough fibres, rapid increases in the shear stress, coordination number and apparent friction coefficient with increasing μ are obtained when μ is less than 0.4, while these three quantities tend to saturate when μ is greater than 0.4. The saturation of the apparent friction coefficient (or the internal friction angle) with increasing μ was also observed in spherical particle systems (Thornton 2000; Suiker & Fleck 2004; Ketterhagen *et al.* 2009). Suiker & Fleck (2004) and Ketterhagen *et al.* (2009) argued that the saturation is caused by the rotation of particles, because the apparent friction coefficient increases sharply with increasing μ when particle rotation is inhibited. In the present work, it is observed that in dense flows, the fibres with friction are interlocked to form agglomerates, which can rotate en masse. The rotation of fibre agglomerates may play a similar role to the rotation of spheres in the previous work (Suiker & Fleck 2004; Ketterhagen *et al.* 2009) in facilitating shear deformation of granular assemblies.

Large fibre deformation (figure 13*c*), large stress and a dense network of force chains (figure 16) are observed for dense flows of rough fibres with $\mu = 0.5$ at $\upsilon = 0.466$. However, for dense flows of smoothed fibres with the same friction coefficient and concentration ($\mu = 0.5$ and $\upsilon = 0.466$), much smaller shear stress, coordination number and apparent friction coefficient are obtained compared with rough fibres, as shown in figure 18. The smoothed surface leads to a reduced chance of fibre interlocking and consequently reduced fibre contacts. As shown in figure 19, the smoothed fibres tend to align in the flow direction with a small number of contact force chains scattered throughout the shear cell. Hence, smoothing the fibre surface, as well as reducing the friction coefficient, decreases the tangential contacts between fibres.

The bond Young's modulus E_b determines the stiffness of fibres. The dependence of shear stress, coordination number and apparent friction coefficient on the bond

https://doi.org/10.1017/jfm.2015.289 Published online by Cambridge University Press

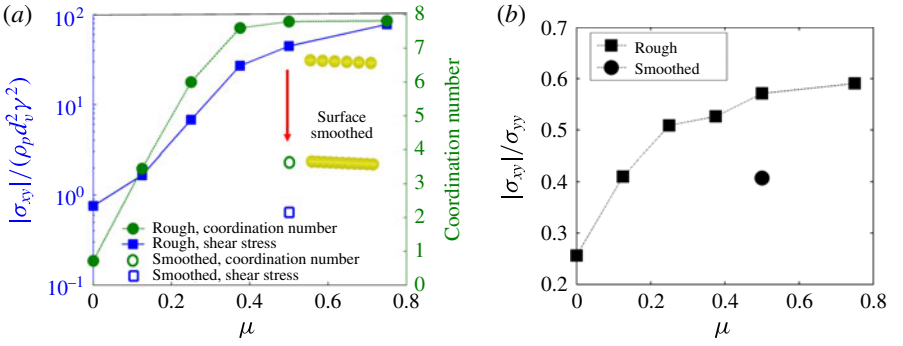


FIGURE 18. (Colour online) (*a*) Shear stress and coordination number and (*b*) apparent friction coefficient as a function of interfibre friction coefficient, μ ($\upsilon = 0.466$, $AR = 6$, $\beta_c = 1.63 \times 10^{-2}$, $E_b = 2.6 \times 10^4$ Pa, $\beta_b = 0$).

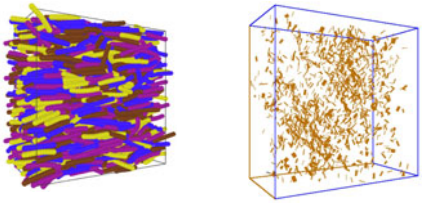


FIGURE 19. (Colour online) A snapshot and corresponding force chains of dense shear flows with smoothed fibres ($\upsilon = 0.466$, $AR = 6$, $\mu = 0.5$, $\beta_c = 1.63 \times 10^{-2}$, $E_b = 2.6 \times 10^4$ Pa, $\beta_b = 0$). The different coloured fibres are for identification purposes only.

Young's modulus for dense flows of frictional rough fibres ($\mu = 0.5$ and $\upsilon = 0.466$) is shown in figure 20. In general, the shear stress and coordination number both increase as E_b increases. In dense flows in a shear cell with a fixed volume, larger fibre stiffness leads to increased contact forces and contact number. It is found that softer frictional fibres tend to roll into round agglomerates under shear, while stiffer fibres are more resistant to bending, remain straight and tend to align with a small angle from the flow direction. The alignment of elongated particles can lead to a reduction in the apparent friction coefficient, as also reported in Guo *et al.* (2013*a*). This reduction occurs because the alignment of the major axes of elongated particles affects the contact force transmission: the normal force transmission (perpendicular to the particle major axis and flow direction) is more favoured than the shear force transmission (parallel to the particle major axis and flow direction). As a result, the extent of increase in the normal stress σ_{yy} is greater than the extent of increase in the shear stress σ_{xy} as the bond Young's modulus E_b increases. Thus, the apparent friction coefficient, i.e. the ratio of σ_{xy} to σ_{yy}, decreases as E_b increases (figure 20*b*). Further, the shear stress, coordination number and apparent friction coefficient of the flexible fibres all approach the values for the rigid fibres as the bond stiffness increases.

The effect of the fibre aspect ratio AR on the shear stress, coordination number and apparent friction coefficient in dense flows of frictional rough fibres ($\mu = 0.5$ and $\upsilon = 0.4$) is shown in figure 21. In dense frictional flows, the elongation of fibres increases the possibility for the fibres to touch their neighbours, therefore increasing

https://doi.org/10.1017/jfm.2015.289 Published online by Cambridge University Press

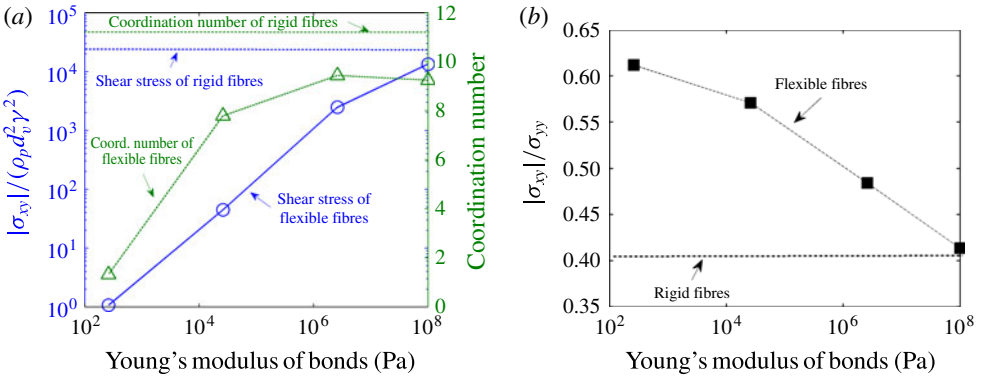


FIGURE 20. (Colour online) (*a*) Shear stress and coordination number and (*b*) apparent friction coefficient as a function of bond Young's modulus ($v = 0.466$, $AR = 6$, $\mu = 0.5$, $\beta_c = 1.63 \times 10^{-2}$, $\beta_b = 0$).

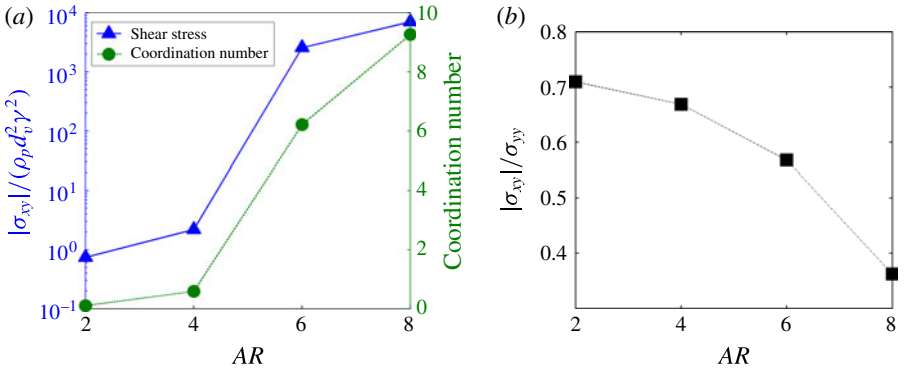


FIGURE 21. (Colour online) (*a*) Shear stress and coordination number and (*b*) apparent friction coefficient as a function of fibre AR ($v = 0.4$, $\beta_c = 1.63 \times 10^{-2}$, $E_b = 1.0 \times 10^8$ Pa, $\beta_b = 0$, $\mu = 0.5$).

contact forces and contact number. As a result, both shear stress and coordination number increase with increasing AR (figure 21*a*). It is observed that sharp increases in the shear stress and coordination number are obtained with intermediate fibre aspect ratios of $4 < AR < 6$, while slow increases are obtained with smaller values of $2 < AR < 4$ and larger values of $6 < AR < 8$. The rapid increase in stress at intermediate ARs may indicate that a critical AR exists for a given solid volume fraction. Jamming occurs with the formation of a dense contact force network at the critical AR. However, the stress remains at a low level before jamming occurs (with smaller ARs), and the stress is large but increases more slowly with AR after the contact force network and jamming are established (with larger ARs). As the fibre AR increases, the alignment of stiff fibres in the flow direction is enhanced. As discussed above, normal force transmission becomes more favoured than shear force transmission due to the alignment, and a larger extent of increase is obtained for the normal stress σ_{yy} than the shear stress σ_{xy} with increasing AR. Thus, the apparent friction coefficient decreases as the AR increases, as shown in figure 21(*b*).

https://doi.org/10.1017/jfm.2015.289 Published online by Cambridge University Press

6. Conclusions

In this study, granular shear flows of dry flexible fibres in the absence of fluid media and gravity have been modelled using the DEM algorithm. The measurement of various quantities (e.g. stress, kinetic and potential energies, deforming parameter, etc.) is made when the shear flow reaches steady state. We have explored the effects of fibre properties, such as bond stiffness, bond damping, friction coefficient, surface roughness and aspect ratio, on fibre deformation, mechanical energy, solid-phase stress, apparent friction coefficient and coordination number in sheared fibre systems. The effective coefficient of restitution, defined as the ratio of postcollisional relative velocity to precollisional relative velocity for a collinear collision of two fibres, increases as the bond stiffness increases and decreases as the bond damping increases. As a result, smaller stresses are obtained for flexible fibres, particularly with bond damping, compared with rigid fibres. Frictionless fibres tend to align with a small angle from the flow direction and the deformation is minimized as the solid volume fraction increases. However, in fibre flows with friction, the interfibre contacts increase significantly as the solid volume fraction increases, leading to significant increases in fibre deformation, PE and solid-phase stress.

In the present work, simulations of shear flows with fixed solid volume fractions are reported. We also performed simulations of stress-controlled shear flows (not shown in this paper), in which a constant pressure was applied to compress a sheared granular bed. It is interesting to point out that with given fibre particle properties and shear rate, the stress–solid volume fraction correlations obtained from the stress-controlled shear flow simulations are the same to those from the present simulations with fixed solid volume fractions.

Jamming is a phenomenon in which a solid-like state is formed to strongly resist the granular flow. Large interfibre contact forces, dense networks of contact force chains and large coordination numbers are observed in a jammed fibre system. Jamming is more likely to occur in flows with larger friction coefficient, rougher surface, larger bond stiffness and larger aspect ratio. In dense flows, the apparent friction coefficient of a bulk material, i.e. the ratio of shear to normal stresses, generally increases with increasing interfibre friction coefficient μ. The apparent friction coefficient saturates and remains approximately constant with increasing μ when μ exceeds a critical value (figure 18*b*) due to the rotation of fibre agglomerates. It is also observed that the apparent friction coefficient of a dense flow decreases as the bond stiffness increases or the fibre aspect ratio increases. This phenomenon is associated with the fibre alignment. More significant alignment of fibre major axes in the flow direction is observed for the stiffer and larger aspect ratio fibres. The alignment affects contact force transmission: normal force transmission (perpendicular to the particle major axis and flow direction) is more favoured than shear force transmission (parallel to the particle major axis and flow direction). As a result, the extent of increase in the normal stress σ_{yy} is greater than the extent of increase in the shear stress σ_{xy} as more significant alignment occurs. Thus, the apparent friction coefficient, i.e. the ratio of σ_{xy} to σ_{yy}, decreases as the bond stiffness and fibre aspect ratio increase.

To conclude, some implications for applications involving the handling of flexible fibre materials are obtained from the present work. The deformation of a flexible fibre allows the conversion of kinetic energy to PE, and the PE can be dissipated in the vibration process. Hence, flexible fibres with appropriate bond stiffness and bond damping may be used as a kinetic energy absorbing material. In the handling of fibres, reduction of the friction coefficient (via adding lubricants or deburring surfaces, for example) reduction of the stiffness (via adding moisture, for example)

https://doi.org/10.1017/jfm.2015.289 Published online by Cambridge University Press

and reduction of the aspect ratio (via milling, for example) can help to reduce the stresses required to make the material flow and the likelihood of jamming. One must be careful, however, to avoid introducing additional cohesive forces or roughness due to moisture or milling respectively. Moisture-induced cohesive interactions between the fibres can promote the formation of large and strong fibre agglomerates, which are likely to cause jamming in fibre discharge, transport and blending operations. Recently, we have studied the effect of moisture-induced cohesion on shear flows of wet fibres using the DEM method, and this study will be published in due course.

Acknowledgements

The authors are grateful for the support of the National Science Foundation (NSF) I/UCRC Center for Particulate and Surfactant Systems, grant 0749481/0749461, as well as the ongoing support of its industry members.

REFERENCES

ACEVEDO, M., ZURIGUEL, I., MAZA, D., PAGONABARRAGA, I., ALONSO-MARROQUIN, F. & HIDALGO, R. C. 2014 Stress transmission in systems of faceted particles in a silo: the roles of filling rate and particle aspect ratio. *Granul. Matt.* **16**, 411–420.

AZÉMA, E. & RADJAÏ, F. 2010 Stress–strain behavior and geometrical properties of packings of elongated particles. *Phys. Rev.* E **81**, 051304.

BABIC, M. 1997 Average balance equations for granular materials. *Intl J. Engng Sci.* **35** (5), 523–548.

BÖRZSÖNYI, T., SZABÓ, B., TÖRÖS, G., WEGNER, S., TÖRÖK, J., SOMFAI, E., BIEN, T. & STANNARIUS, R. 2012*a* Orientational order and alignment of elongated particles induced by shear. *Phys. Rev. Lett.* **108**, 228302.

BÖRZSÖNYI, T., SZABÓ, B., WEGNER, S., HARTH, K., TÖRÖK, J., SOMFAI, E., BIEN, T. & STANNARIUS, R. 2012*b* Shear induced alignment and dynamics of elongated granular particles. *Phys. Rev.* E **86**, 051304.

CAMPBELL, C. S. 2002 Granular shear flows at the elastic limit. *J. Fluid Mech.* **465**, 261–291.

CAMPBELL, C. S. 2005 Stress-controlled elastic granular shear flows. *J. Fluid Mech.* **539**, 273–297.

CAMPBELL, C. S. 2006 Granular material flows – an overview. *Powder Technol.* **162**, 208–229.

CAMPBELL, C. S. 2011 Elastic granular flows of ellipsoidal particles. *Phys. Fluids* **23**, 013306.

CAMPBELL, C. S. & GONG, A. 1986 The stress tensor in a two-dimensional granular shear flow. *J. Fluid Mech.* **164**, 107–125.

CLEARY, P. W. 2008 The effect of particle shape on simple shear flows. *Powder Technol.* **179**, 144–163.

GOLDHIRSCH, I. 2010 Stress, stress asymmetry and couple stress: from discrete particles to continuous fields. *Granul. Matt.* **12**, 239–252.

GOLDHIRSCH, I. 2003 Rapid granular flows. *Annu. Rev. Fluid Mech.* **35**, 267–293.

GOLDSHTEIN, A. & SHAPIRO, M. 1995 Mechanics of collisional motion of granular materials. Part I. General hydrodynamic equations. *J. Fluid Mech.* **282**, 75–114.

GUISES, R., XIANG, J., LATHAM, J. P. & MUNJIZA, A. 2009 Granular packing: numerical simulation and the characterization of the effect of particle shape. *Granul. Matt.* **11**, 281–292.

GUO, Y. 2010 A coupled DEM/CFD analysis of die filling process. PhD thesis, The University of Birmingham, UK, pp. 40–41.

GUO, Y., WASSGREN, C., HANCOCK, B., KETTERHAGEN, W. & CURTIS, J. 2013*a* Granular shear flows of flat disks and elongated rods without and with friction. *Phys. Fluids* **25**, 063304.

GUO, Y., WASSGREN, C., HANCOCK, B., KETTERHAGEN, W. & CURTIS, J. 2013*b* Validation and time step determination of discrete element modeling of flexible fibers. *Powder Technol.* **249**, 386–395.

https://doi.org/10.1017/jfm.2015.289 Published online by Cambridge University Press

GUO, Y., WASSGREN, C., KETTERHAGEN, W., HANCOCK, B., JAMES, B. & CURTIS, J. 2012 A numerical study of granular shear flows of rod-like particles using the discrete element method. *J. Fluid Mech.* **713**, 1–26.

HIDALGO, R. C., ZURIGUEL, I., MAZA, D. & PAGONABARRAGA, I. 2010 Granular packings of elongated faceted particles deposited under gravity. *J. Stat. Mech.* **2010**, P06025.

HUA, X., CURTIS, J., HANCOCK, B., KETTERHAGEN, W. & WASSGREN, C. 2013 The kinematics of non-cohesive, sphero-cylindrical particles in a low-speed, vertical axis mixer. *Chem. Engng Sci.* **101**, 144–164.

HUTHMANN, M., ASPELMEIER, T. & ZIPPELIUS, A. 1999 Granular cooling of hard needles. *Phys. Rev.* E **60**, 654–659.

JENKINS, J. T. 2006 Dense shearing flows of inelastic disks. *Phys. Fluids* **18**, 103307.

JOHNSON, K. L. 1985 *Contact Mechanics*. Cambridge University Press.

JOHNSON, P. C. & JACKSON, R. 1987 Frictional-collisional constitutive relations for granular materials with applications to plane shearing. *J. Fluid Mech.* **176**, 67–93.

JOHNSON, P. C., NOTT, P. & JACKSON, R. 1990 Frictional-collisional equations of motion for particulate flows and their applications to plane shearing. *J. Fluid Mech.* **210**, 501–535.

JOP, P., FORTERRE, Y. & POULIQUEN, O. 2006 A constitutive law for dense granular flows. *Nature* **441**, 727–730.

KETTERHAGEN, W., CURTIS, J., WASSGREN, C. & HANCOCK, B. 2009 Predicting the flow mode from hoppers using the discrete element method. *Powder Technol.* **195**, 1–10.

LANGSTON, P., KENNEDY, A. R. & CONSTANTIN, H. 2015 Discrete element modeling of flexible fibre packing. *Comput. Mater. Sci.* **96**, 108–116.

LAVENSON, D. M., TOZZI, E. J., MCCARTHY, M. J. & POWELL, R. L. 2011 Yield stress of pretreated corn stover suspensions using magnetic resonance imaging. *Biotechnol. Bioengng* **108**, 2312–2319.

LEES, A. W. & EDWARDS, S. F. 1972 The computer study of transport processes under extreme conditions. *J. Phys. C: Solid State Phys.* **5**, 1921–1929.

LINDSTROM, S. B. & UESAKA, T. 2007 Simulation of the motion of flexible fibers in viscous fluid flow. *Phys. Fluids* **19**, 113307.

LUMAY, G. & VANDEWALLE, N. 2006 Experimental study of the compaction dynamics for two-dimensional anisotropic granular materials. *Phys. Rev.* E **74**, 021301.

LUN, C. K. K., SAVAGE, S. B., JEFFREY, D. J. & CHEPURNIY, N. 1984 Kinetic theories for granular flow: inelastic particles in Couette flow and slightly inelastic particles in a general flow field. *J. Fluid Mech.* **140**, 223–256.

MONTANERO, J. M., GARZO, V., SANTOS, A. & BREY, J. J. 1999 Kinetic theory of simple granular shear flows of smooth hard spheres. *J. Fluid Mech.* **389**, 391–411.

NING, Z. & MELROSE, J. R. 1999 A numerical model for simulating mechanical behavior of flexible fibers. *J. Chem. Phys.* **111**, 10717–10726.

PEÑA, A. A., GARCÍA-ROJO, R. & HERRMANN, H. J. 2007 Influence of particle shape on sheared dense granular media. *Granul. Matt.* **9**, 279–291.

POTYONDY, D. O. & CUNDALL, P. A. 2004 A bonded-particle model for rock. *Int. J. Rock Mech. Min. Sci.* **41**, 1329–1364.

POULIQUEN, O. & FORTERRE, Y. 2009 A non-local rheology for dense granular flows. *Phil. Trans. R. Soc. Lond.* A **367**, 5091–5107.

REDDY, K. A., KUMARAN, V. & TALBOT, J. 2009 Orientational ordering in sheared inelastic dumbbells. *Phys. Rev.* E **80**, 031304.

ROSS, R. F. & KLINGENBERG, D. J. 1997 Dynamic simulation of flexible fibers composed of linked rigid bodies. *J. Chem. Phys.* **106**, 2949–2960.

STICKEL, J. J., KNUTSEN, J. S., LIBERATORE, M. W., LUU, W., BOUSFIELD, D. W., KLINGENBERG, D. J., SCOTT, C. T., ROOT, T. W., EHRHARDT, M. R. & MONZ, T. O. 2009 Rheology measurements of a biomass slurry: an inter-laboratory study. *Rheol. Acta* **48**, 1005–1015.

SUIKER, A. S. & FLECK, N. A. 2004 Frictional collapse of granular assemblies. *Trans. ASME J. Appl. Mech.* **71**, 350–358.

https://doi.org/10.1017/jfm.2015.289 Published online by Cambridge University Press

THORNTON, C. 2000 Numerical simulations of deviatoric shear deformation of granular media. *Géotechnique* **50**, 43–53.

THORNTON, C. & YIN, K. K. 1991 Impact of elastic spheres with and without adhesion. *Powder Technol.* **65**, 153–165.

WEGNER, S., STANNARIUS, R., BOESE, A., ROSE, G., SZABO, B., SOMFAI, E. & BORZSONYI, T. 2014 Effects of grain shape on packing and dilatancy of sheared granular materials. *Soft Matt.* **10**, 5157–5167.

WEINHART, T., HARTKAMP, R., THORNTON, A. R. & LUDING, S. 2013 Coarse-grained local and objective continuum description of three-dimensional granular flows down an inclined surface. *Phys. Fluids* **25**, 070605.

WEINHART, T., THORNTON, A. R., LUDING, S. & BOKHOVE, O. 2012 From discrete particles to continuum fields near a boundary. *Granul. Matt.* **14**, 289–294.

WOUTERSE, A., LUDING, S. & PHILIPSE, A. P. 2009 On contact numbers in random rod packings. *Granul. Matt.* **11**, 169–177.

WU, J. & AIDUN, C. K. 2010 A method for direct simulation of flexible fiber suspensions using lattice Boltzmann equation with external boundary force. *Intl J. Multiphase Flow* **36**, 202–209.

YAMAMOTO, S. & MATSUOKA, T. 1993 A method for dynamic simulation of rigid and flexible fibers in a flow field. *J. Chem. Phys.* **98**, 644–650.

https://doi.org/10.1017/jfm.2015.289 Published online by Cambridge University Press